# FORMATION AND PROPAGATION OF LIMITED DIFFRACTION BEAMS

Jian-yu Lu and James F. Greenleaf

Biodynamics Research Unit, Department of Physiology and Biophysics
Mayo Clinic/Foundation
Rochester, MN 55905

## INTRODUCTION

Since the first discovery of localized waves (focused wave mode) in 1983[1] and limited diffraction beams (Bessel beams) in 1987,[2] great advancement in both theory and experiment of these beams have been achieved.[3–6] Generalization of the limited diffraction beams and their applications to medical ultrasonic imaging, biological tissue characterization, and ultrasonic nondestructive evaluation of materials have also been reported.[7–15]

In this paper, formation of the limited diffraction beams by transducer elements and propagation of the resulting two- and three-dimensional waves will be shown. The limited diffraction beams are pencil-like over large depth of field even if they are approximately produced with a finite aperture. In next section we will give a brief review of the theory of the limited diffraction beams. Then, we will show both two- and three-dimensional formation and propagation of the limited diffraction beams. Finally, we have a short discussion and conclusion.

## THEORETICAL PRELIMINARIES

One of the special families of solutions of the n-dimensional loss-free, isotropic/homogeneous wave equation is given by[15]

$$\Phi(x_1, x_2, \cdots, x_n; t) = f(s), \tag{1}$$

*Acoustical Imaging, Volume 20* Edited by Y. Wei
and B. Gu, Plenum Press, New York, 1993

where

$$s = \sum_{j=1}^{n-1} D_j x_j + D_n(x_n - c_1 t), \quad (n \geq 1), \tag{2}$$

and where

$$c_1 = \pm c \sqrt{1 + \sum_{j=1}^{n-1} D_j^2 / D_n^2}, \quad (n \geq 1). \tag{3}$$

$D_j$ are complex parameters which are independent of spatial and time variables ($x_j$ $(j = 1, 2, \cdots, n)$ and $t$), and $f(s)$ is any complex function (well-behaved) of $s$.

If $c_1$ in Eq. (2) is real, f(s) represents a limited diffraction wave propagating along axis, $x_n$, at the phase velocity of $c_1$, in an n-dimensional space, i.e., traveling with the wave, one sees a complex wave pattern unchanged in both amplitude and phase. The "$\pm$" term in Eq. (3) represents forward and backward propagating waves, respectively. In the following, we consider forward going waves only. For backward going waves, the results are similar.

Follow the procedures in Reference 15 or 11 (i.e., choose the function forms of the parameters, $D_j$, and integrate over some of their arguments), we obtain the $J_0$ Bessel beam[2] and the zeroth-order X wave[11]

$$J_0(\alpha r) e^{i\beta z - i\omega t} \tag{4}$$

and

$$\frac{1}{a_0} b(t) * \frac{a_0}{\sqrt{(r \sin\zeta)^2 + [a_0 - i \cos\zeta (z - c_1 t)]^2}}, \tag{5}$$

respectively, where $J_0(\alpha r)$ is the zeroth-order Bessel function of the first kind, $\alpha$ is a constant, $r = \sqrt{x^2 + y^2}$ represents radial distance, $\beta = \sqrt{(\omega/c)^2 - \alpha^2}$, $\omega$ is angular frequency, $c$ is speed of sound or speed of light, $t$ is time, $a_0$ is a constant, $b(t)$ is an impulse response of a transducer and its associated electronics, $\zeta$ is an angle between sidelobe of X wave and surface of transducer, and $c_1 = c/\cos\zeta$ for the X wave. If the $J_0$ Bessel beam and the zeroth-order X wave are truncated to a finite aperture with a radius, $a$, the depths of field (propagation distances over which the waves are approximately unchanged) are given by[2,11,15]

$$Z_{Bmax} = a \sqrt{\left(\frac{\omega}{\alpha c}\right)^2 - 1} \tag{6}$$

and

$$Z_{Xmax} = a \cot\zeta, \tag{7}$$

respectively.

In the following, it will be shown how a $J_0$ Bessel beam and a zeroth-order X wave are formed by an annular array transducer element by element and propagate in water over large distances.

## FORMATION AND PROPAGATION OF LIMITED DIFFRACTION BEAMS

Simulations of the formation and propagation of the limited diffraction beams were performed with the Rayleigh-Sommerfeld formulation of diffraction.[16] The aperture geometry of wave sources (transducers) were assumed to be the same as that of an experimental

transducer. The driving waveforms[7,12] for producing the $J_0$ Bessel beam and zeroth-order X wave will be described in the following. The wave fields will be displayed in two- and three-dimensional format.[17]

The experiment setup for measuring acoustic wave fields is shown in Fig. 1. A polynomial waveform generator produced a tone burst or short electric pulses. These electric signals were amplified by a RF power amplifier to excite the transducer element by element. The acoustic wave fields produced in water were measured by a 0.5 mm diameter calibrated hydrophone. Output signals of the hydrophone were amplified and digitized, and then stored in a hard disk. The hydrophone can be scanned along two axes as shown in Fig. 1 to sample either pulse or CW wave fields. It can also be placed at various depths along the wave axis. The transmission of the signals was synchronized to the scan of the hydrophone, and data were transferred to a SUN SPARCstation for further processing and display.

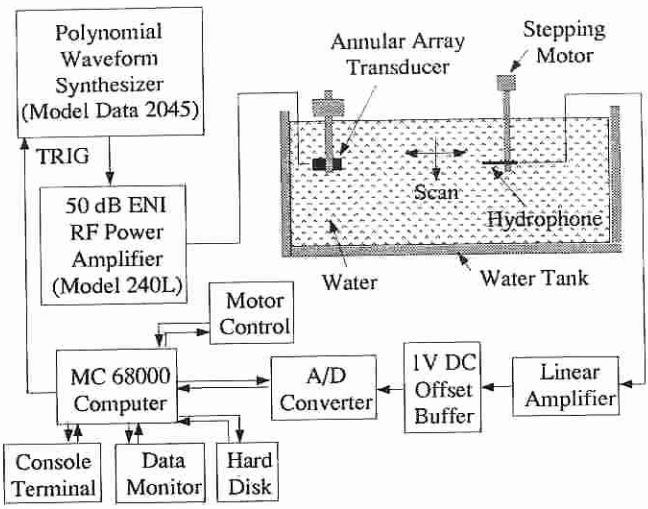


**Figure 1.** Experiment block diagram for measuring acoustic wave fields in water. The system can measure both CW and pulse wave fields at various depths.

The transducer used in the experiment is a 10–element annular array, which was described in detail in References 9 and 12. The transducer has a diameter of 50 mm, a central frequency of 2.5 MHz, and a $-6$ dB pulse-echo (two-way) bandwidth of about 50% of the central frequency.

Figure 2 shows analytic envelopes of experimentally measured wave fields in a plane along the axis. The wave fields were obtained by increasing the number of excited transducer elements to form a CW $J_0$ Bessel beam. Panel (1) represent the wave field when only central element was excited and Panel (10) is the wave field when all the elements were excited simultaneously (Panel (n) shows the wave field when central n elements were excited simultaneously). Each panel was normalized to its maximum and the wave fields were measured from 5 mm to 210 mm away from the surface of the transducer. The elements were driven with alternate voltage polarity and the relative amplitude of the

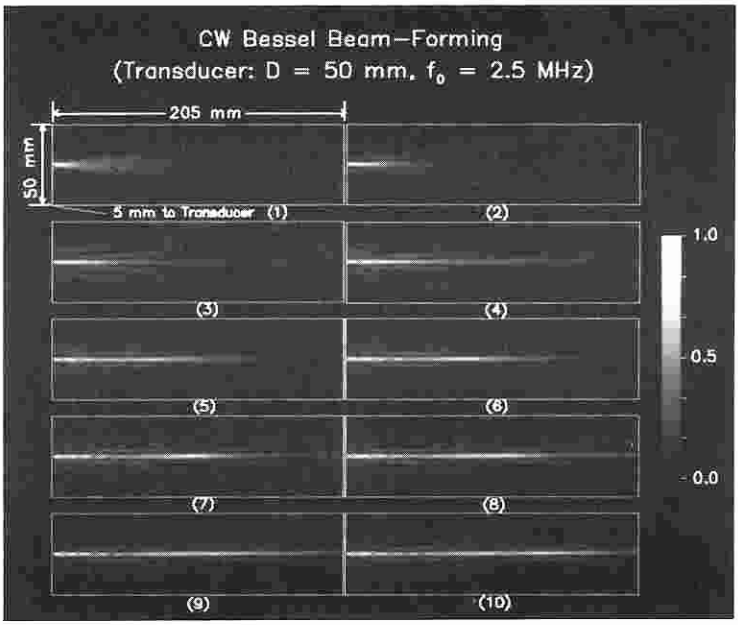


**Figure 2.** Formation of a CW $J_0$ Bessel beam in water. Panels (1) to (10) represent the analytic envelope of the wave fields produced when increasing the number of the excited transducer elements, beginning from the central element. The wave fields were measured in a plane along the axis and the image in each panel was normalized to its maximum. The transducer is an annular array with 10 elements. Its diameter is 50 mm and central frequency is 2.5 MHz. The $-6$ dB pulse-echo (two-way) bandwidth of the transducer is about 50% of its central frequency. All panels of images begin 5 mm away from the surface of the transducer. The panel size of the beams is 205 mm (axial) $\times$ 50 mm (lateral).

driving voltages corresponded to the peaks of the lobes of the $J_0$ Bessel function (with the scaling factor $\alpha = 1202.45\ m^{-1}$ ).

Figure 3 is the same as Fig. 2 except that a pulse of about one-and-half cycles (2.5 MHz central frequency) was used to drive the transducer. The pulse wave fields were measured at an axial distance of 100 mm (Z/D = 2.0 where Z is axial distance and D = 50 mm is the diameter of the transducer). Figure 4 is a three-dimensional representation of images in Fig. 3. The two-dimensional wave fields in Fig. 3 were rotated around the wave axis to construct three-dimensional wave fields (since the transducer is axially symmetric, the three-dimensional fields should also be symmetric). The three-dimensional wave fields were thresholded at a level of $-10$ dB down from the maximum of each panel of Fig. 3 to form binary images (anything below $-10$ dB is "0", and above is "1"). The three-dimensional binary images were contour extracted and surface rendered for the display of the three-dimensional wave objects using commercially available software package ANALYZE$^{TM}$. Figure 5 shows line plots of images in Fig. 3. The lateral distribution of the maxima of the wave fields in the lines parallel to the wave axis in each panel are shown. This emphasizes the maximum sidelobes of the pulses (the sidelobes are essential to the contrast of medical imaging).

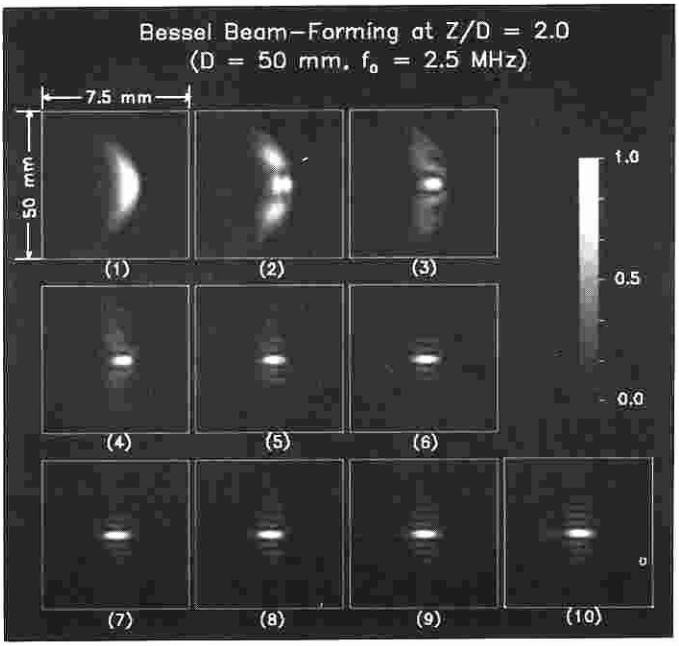


**Figure 3.** The same format as Fig. 2 for the formation of a pulse $J_0$ Bessel beam (the transducer was driven by a one-and-half cycle short pulse) obtained at a depth of 100 mm. The panel size of the beams is 7.5 mm (axial) × 50 mm (lateral).

Figures 6 to 8 show the beam-forming of a zeroth-order X wave at a distance of 170 mm (Z/D = 3.4) and correspond in format to Figs. 3 to 5, respectively. The X wave was produced with drive functions calculated from Eq. (5) by setting $b(t)$ as a $\delta$-function, $z = 0$, and $r$ as the mean diameter of each transducer element. The contants $a_0$ and $\zeta$ are 0.05 mm and 4°, respectively.

Figure 9 shows the propagation of the pulse $J_0$ Bessel beam from 25 mm to 300 mm (Z/D = 0.5 to 6.0), with a depth interval of 25 mm (Z/D = 0.5). The beam was formed with simultaneous excitation of all of the transducer elements. The pulse $J_0$ Bessel beam stays well in focus (full width at half maximum main beamwidth is about 2.54 mm[7]) over a large depth of field (216 mm calculated from Eq. (6)). Fig. 10 is the three-dimensional representation of images in Fig. 9. It was obtained with the same procedures as those for producing Fig. 4. Figure 11 is the line plots of the images in Fig. 9 and shows sidelobes of the pulse Bessel beam. (Figures 9 to 11 have similar formats as Figs. 3 to 5, respectively.)

Figures 12 to 14 represent the zeroth-order X wave propagating from 25 mm to 400 mm (Z/D = 0.5 to 8.0) with a depth interval of 25 mm (Z/D = 0.5) and correspond in format to Figs. 9 to 11, respectively. The X wave has a depth of field of about 358 mm (calculated from Eq. (7)) with a lateral and axial full width at half maximum of about 4.7 mm and 0.65 mm, respectively.[12]

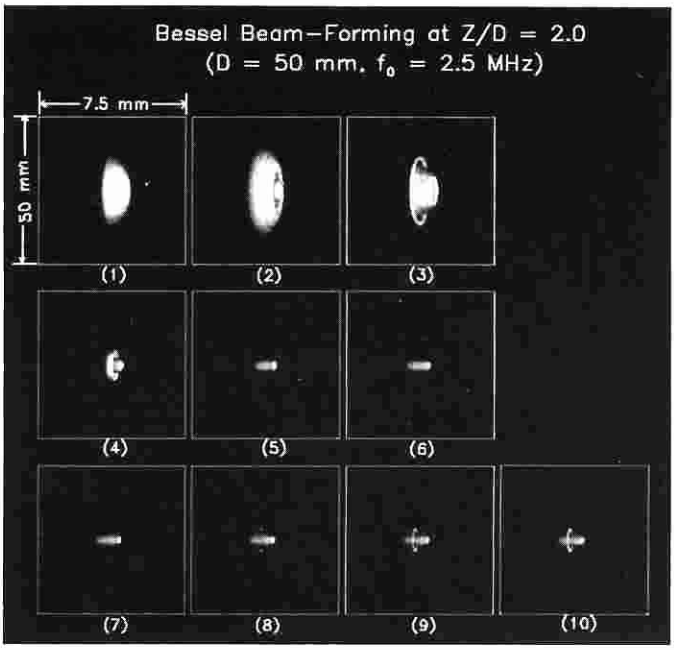


**Figure 4.** Three-dimensional representation of pulses in Fig. 3. The two-dimensional wave fields in Fig. 3 were rotated around the wave axis to construct three-dimensional wave fields. The three-dimensional wave fields were thresholded at a level of −10 dB down from the maximum of each panel of Fig. 3 to form binary images. The three-dimensional binary images were contour extracted and surface rendered for the display of three-dimensional wave objects.

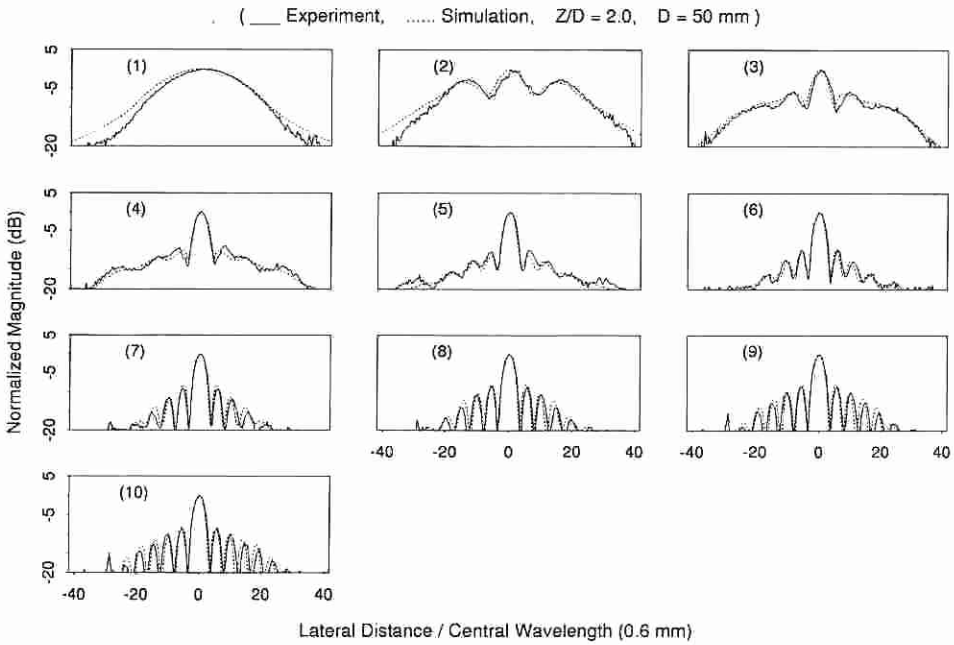


Fig. 5. Line plots of beams in Fig. 3. The maxima of wave fields in lines parallel to the wave axes (axial axes) were plotted over the lateral distance. Full lines and dotted lines represent the experiment and simulation results, respectively.

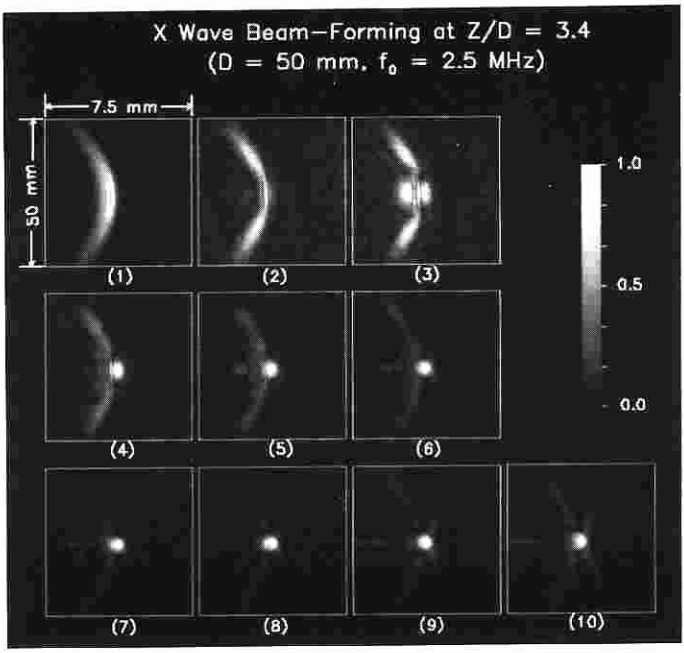


**Figure 6.** Formation of a zeroth-order X wave in water. The wave fields were measured at a depth of 170 mm. The drive waveforms for the transducer elements are calculated from Eq. (5) by setting $b(t)$ as a $\delta$-function, $z = 0$, and $r$ as the mean diameter of each transducer element. The constants $a_0$ and $\zeta$ are 0.05 mm and 4°, respectively. The display format of each panel is the same as that of Fig. 3.

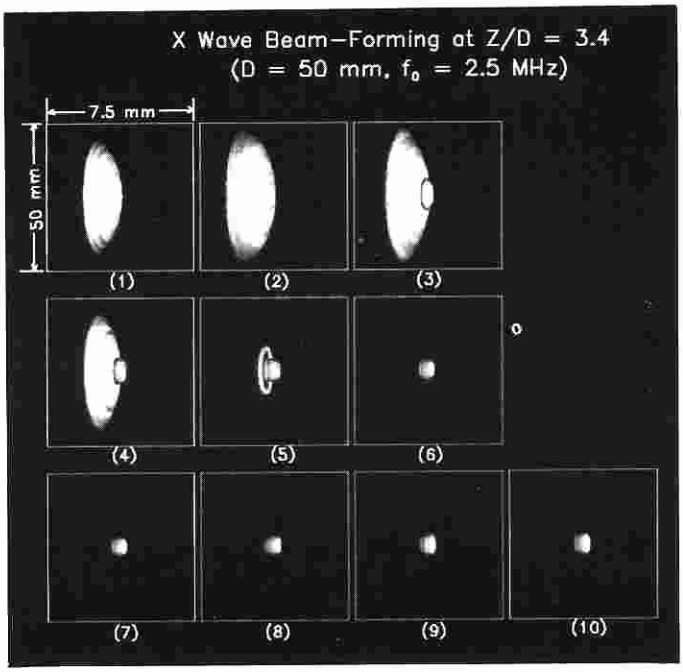


**Figure 7.** Three-dimensional representation of beams in Fig. 6. The display format of each panel is the same as that of Fig. 4.

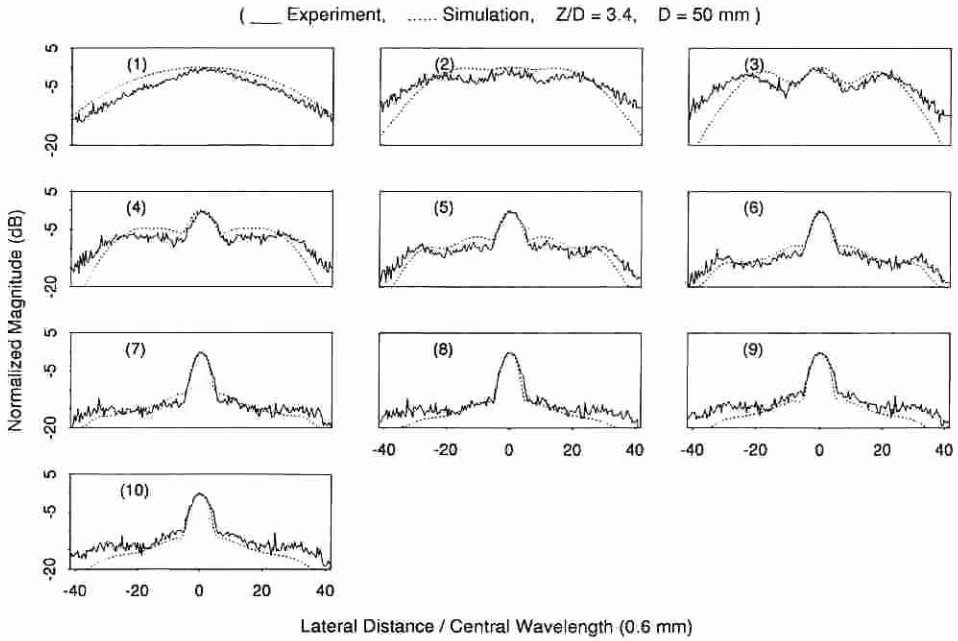


**Figure 8.** Line plots of images in Fig. 6. The display format of each panel is the same as that of Fig. 5.

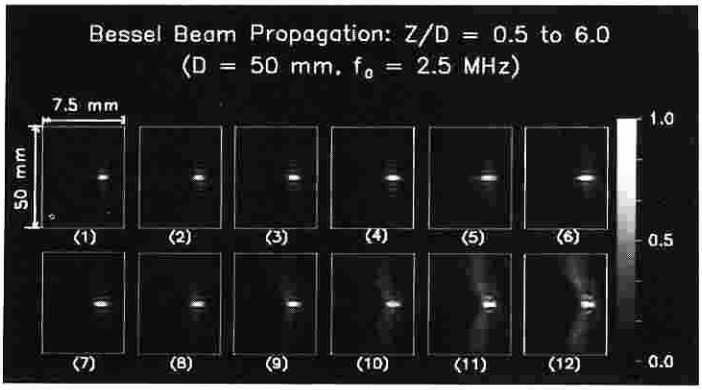


**Figure 9.** Propagation of the pulse $J_0$ Bessel beam from Z = 25 mm (Panel (1)) to 300 mm (Panel (12)) (Z/D = 0.5 to 6.0, where D = 50 mm is the diameter of the transducer) with a depth interval of 25 mm (Z/D = 0.5). The pulses were produced with the 10 transducer elements excited simultaneously. The display format of each panel is the same as that in Fig. 3.

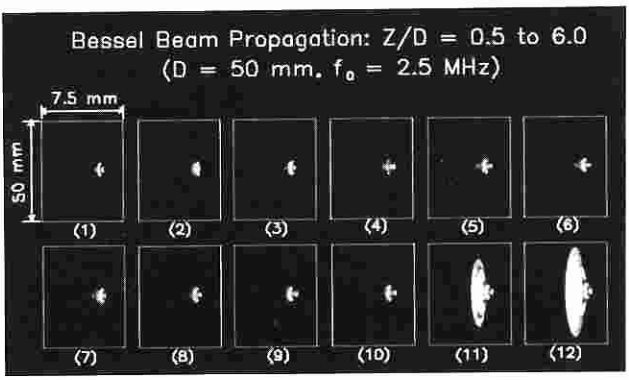


**Figure 10.** Three-dimensional representation of beams in Fig. 9. The display format of each panel is the same as that of Fig. 4.

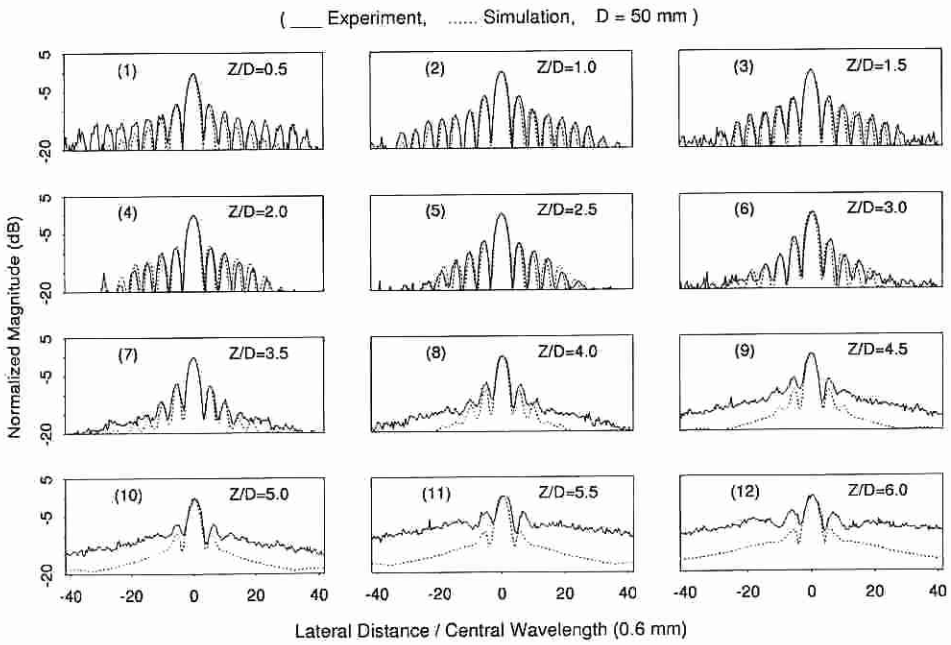


**Figure 11.** Line plots of images in Fig. 9. The display format of each panel is the same as that of Fig. 5.

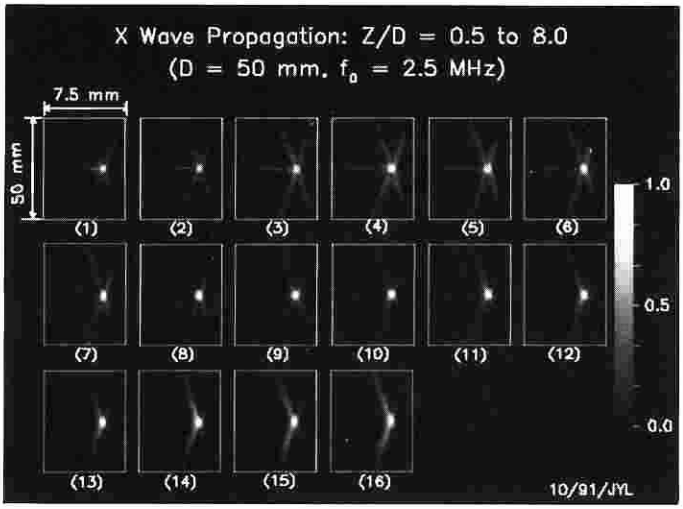


**Figure 12.** Propagation of the zeroth-order X wave from Z = 25 mm (Panel (1)) to 400 mm (Panel (16)) (Z/D = 0.5 to 8.0, where D = 50 mm is the diameter of the transducer) with a depth interval of 25 mm (Z/D = 0.5). The wave fields were produced with the 10 transducer element excited simultaneously. The display format of each panel is the same as that in Fig. 3.

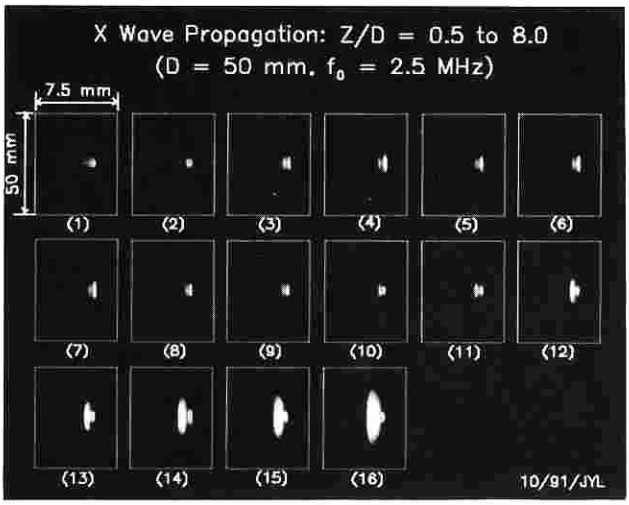


**Figure 13.** Three-dimensional representation of beams in Fig. 12. The display format of each panel is the same as that of Fig. 4.

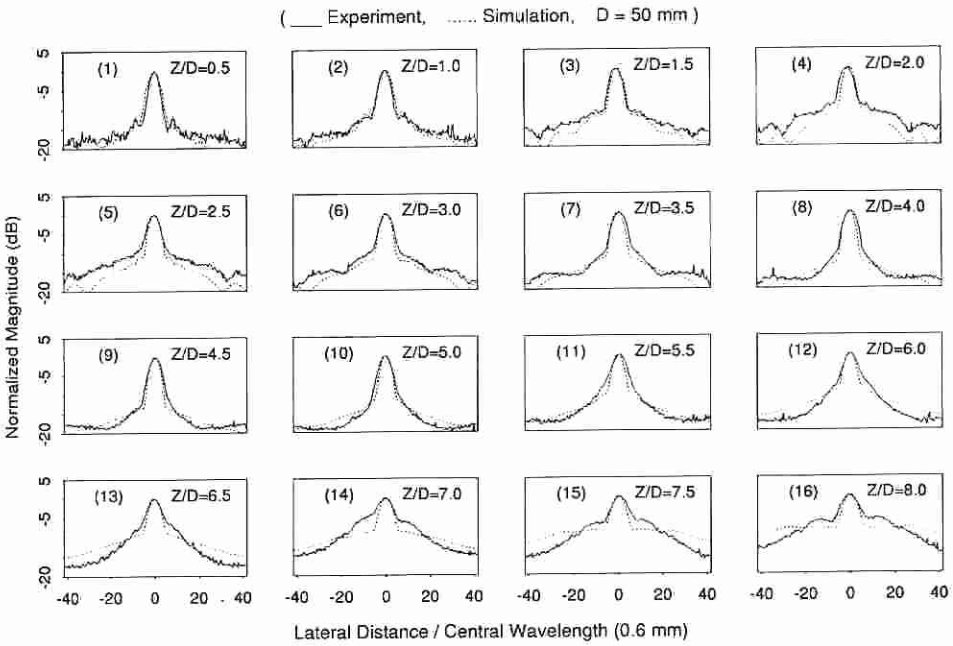


**Figure 14.** Line plots of images in Fig. 12. The display format of each panel is the same as that of Fig. 5.

## DISCUSSION

Figures 2 to 8 show that the limited diffraction beams ($J_0$ Bessel beam and the zeroth-order X wave) are formed by interference of the wave fields produced from the transducer elements. The center element produces a beam which has a cone-like shape (Panel (1) in Fig. 2). With the central two elements (Panel (2) in Fig. 2), the cone is divided into three sub-cones. Finally, with all the elements (Panel (10) in Fig. 2), a perfect line focusing beam is formed over a large depth of field. The two-dimensional pulse $J_0$ Bessel beam and the zeroth-order X wave (Figs. 3 and 6) are formed in a similar way as the CW $J_0$ Bessel beam in Fig. 2. Three-dimensional beams give a clear view of the sizes of the beams (Figs. 4 and 7). Line plots (Figs. 5 and 8) compare the simulations to experiment.

The propagation of the two- and three-dimensional pulse $J_0$ Bessel beam and the zeroth-order X wave (Figs. 9 to 14) shows that the limited diffraction beams have unique ability to maintain small main beam-widths (2.54 mm and 4.7 mm for the Bessel beam and X wave[7,12], respectively) while propagating over large depths of field (216 mm and 358 mm for the Bessel beam and X wave, respectively). If the medium is loss-free, homogeneous and isotropic, one can expect that the limited diffraction beams produced with an infinite aperture (for example, those given by the mathematical solutions in Eqs. (1), (4) and (5)) will propagate to infinite distance without spreading.

In addition to the main beam component, the limited diffraction beams have higher sidelobes as compared to conventional focused beams at their focuses (sidelobes of a focused Gaussian beam was shown in Reference 9). The sidelobes will degrade the contrast of medical images. One way to overcome the effects of the sidelobes would be a pulse-

echo imaging system which transmits with a limited diffraction beam and receives with a conventional dynamically focused beam.

The small deviations between simulations and experiment in the formation of the limited diffraction beams (see Figs. 5 and 8) are due to the difference between the size of some electrodes of the transducer in experiment and simulations. The differences of simulations and experiment of the propagation of the limited diffraction beams (see Figs. 11 and 14) at larger distances (where the signal-to-noise ratio decreases) are caused by the high noise of our prototype electronic system used to produce the limited diffraction beams.

## CONCLUSION

The limited diffraction beams have small main beamwidth over a very large depth of field (pencil-like). They can be formed in such a way that best balances the beam spreading and depth of field. It is expected that these beams could be applied to various wave related areas, such as, acoustics, microwaves, electromagnetics, and optics, whenever both high resolution and large depth of field are required.

## ACKNOWLEDGMENTS

The authors thank Randall R. Kinnick for constructing the electronic circuits to drive the transducer. The authors appreciate the secretarial assistance of Elaine C. Quarve and the graphic assistance of Christine A. Welch. This work was supported in part by grants CA 43920 and CA 54212 from the National Institutes of Health.

## REFERENCES

1. J.B. Brittingham, "Focus wave modes in homogeneous Maxwell's equations: transverse electric mode," *J. Appl. Phys.*, 54(3):1179–1189 (1983).
2. J. Durnin, "Exact solutions for nondiffracting beams. I. The scalar theory," *J. Opt. Soc. Am.*, 4(4):651–654 (1987).
3. R.W. Ziolkowski, D.K. Lewis, and B.D. Cook, "Evidence of localized wave transmission," *Phys. Rev. Lett.*, 62(2):147–150 (Jan. 9, 1989).
4. G. Indebetow, "Nondiffracting optical fields: some remarks on their analysis and synthesis," *J. Opt. Soc. Am. A*, 6(1):150–152 (Jan., 1989).
5. D.K. Hsu, F.J. Margetan, and D.O. Thompson, "Bessel beam ultrasonic transducer: fabrication method and experimental results," *Appl. Phys. Lett.*, 55(20):2066–2068 (Nov. 13, 1989).
6. J.A. Campbell and S. Soloway, "Generation of a nondiffracting beam with frequency independent beam width," *J. Acoust. Soc. Am.*, 88(5):2467–2477 (Nov., 1990).
7. J-y. Lu and J.F. Greenleaf, "Ultrasonic nondiffracting transducer for medical imaging," *IEEE Trans. Ultrason., Ferroelec., Freq. Contr.*, 37(5):438–447 (Sept., 1990).
8. J-y. Lu, and J.F. Greenleaf, "Evaluation of a nondiffracting transducer for tissue characterization," [IEEE 1990 Ultrasonics Symposium, Honolulu, HI, Dec. 4–7, 1990], *IEEE 1990 Ultrason. Symp. Proc.*, 90CH2938–9, 2:795–798 (1990).
9. J-y. Lu and J.F. Greenleaf, "Pulse-echo imaging using a nondiffracting beam transducer," *Ultrasound Med. Biol.*, 17(3):265–281 (May, 1991).

10. J-y. Lu and J.F. Greenleaf, "Theory and acoustic experiments of nondiffracting X waves," [IEEE 1991 Ultrasonics Symposium, Lake Buena Vista, FL, December 8–11, 1991], *IEEE 1991 Ultrason. Symp. Proc.*, 91CH3079–1, 2:1155–1159 (1991).
11. J-y. Lu and J.F. Greenleaf, "Nondiffracting X waves — exact solutions to free-space scalar wave equation and their finite aperture realizations," *IEEE Trans. Ultrason., Ferroelec, Freq. Cont.*, 39(1):19–31 (Jan., 1992).
12. J-y. Lu and J.F. Greenleaf, "Experimental verification of nondiffracting X waves," *IEEE Trans. Ultrason., Ferroelec., Freq. Contr*, 39(3):441–446 (May, 1992).
13. J-y. Lu and J.F. Greenleaf, "Nondestructive evaluation of materials with a $J_0$ Bessel transducer," [17th International Symposium on Ultrasonic Imaging and Tissue Characterization, Arlington, VA, June 1–3, 1992], *Ultrason. Imaging*, 14(2):203–204 (April, 1992) (abs.).
14. J-y. Lu and J.F. Greenleaf, "Sidelobe reduction of nondiffracting pulse-echo images by deconvolution," [17th International Symposium on Ultrasonic Imaging and Tissue Characterization, Arlington, VA, June 1–3, 1992], *Ultrason. Imaging*, 14(2):203 (April, 1992) (abs.).
15. J-y. Lu and J.F. Greenleaf, "Diffraction-limited beams and their applications for ultrasonic imaging and tissue characterization," [SPIE's 1992 International Symposium on Optical Applied Science and Engineering, San Diego, CA, July 19–24, 1992], *New Developments in Ultrasonic Transducers and Transducer Systems*, F.L. Lizzi, ed. (Invited paper).
16. J.W. Goodman, *Introduction to Fourier Optics*. McGraw-Hill, New York, chs. 2–4 (1968).
17. J-y. Lu, T. Kinter, and J.F. Greenleaf, "Measurement and dynamic display of acoustic wave pulses," [IEEE 1989 Ultrasonics Symposium, Montreal, Quebec, Canada, Oct. 3–6, 1989], *IEEE 1989 Ultrason. Symp. Proc.*, 89CH2791–2, 1:673–676 (1989).